Classification
Physics Abstracts
07.80 — 34.80 — 81.70

Energy-filtering transmission electron microscopy in materials science

Ludwig Reimer, Inge Fromm, Christoph Hülk and Reinhold Rennekamp

Physikalisches Institut, Universität Münster, Wilhelm-Klemm-Strasse 10, 4400 Münster, Germany

Abstract. — Energy-filtering transmission electron microscopy (EFTEM) with an imaging filter lens can combine the modes of electron spectroscopic imaging (ESI) and electron spectroscopic diffraction (ESD), and different modes can be used to record an electron energy-loss spectrum (EELS). Therefore, an EFTEM can make full use of the elastic and inelastic electron-specimen interactions. This review summarizes the possibilities of EFTEM for applications in materials science.

1. Introduction.

Transmission electron microscopy (TEM) lives from the elastic scattering of electrons. Inelastic scattering with energy losses is mostly troublesome due to the chromatic aberration and the delocalization of inelastic scattering processes. Boersch [1] and Möllenstedt and Rang [2] first used zero-loss filtering of images and diffraction patterns by means of a grid or increasing the potential at the central electrode of a electrostatic lens but aberrations in this type of lenses limited their use. A cylindrical electrostatic lens (Möllenstedt analyzer [3]), retarding field spectrometers [4] and a Wien filter [5, 6] have been used in many laboratories for the investigation of the plasmon-losses in an electron energy-loss spectrum (EELS) which first have been reported by Rudberg [7] and Ruthemann [8]. The latter showed already the existence of edges by inner-shell ionization and Hillier and Baker [9] started the first attempt of an elemental microanalysis before EELS became a routine method [10, 11] especially with magnetic prism spectrometers below the final image.

In 1962 Castaing and Henry [12] at first demonstrated a filter lens by a combination of a magnetic prism and an electrostatic mirror which has been further developed [13] and is now in widespread use in a commercial instrument [14]. The limitation to acceleration voltages of the order of 80 − 100 kV due to an increased risk of electrical breakdowns at higher voltages has been overcome by the use of pure magnetic Ω-filters first proposed in the thesis of Sénoussi (Paris-Orsay 1971) which also allow to correct for the second order aberration [15-17].

The installation of such a filter lens in the electron-optical column of a transmission electron microscope allows to combine several modes of electron spectroscopic imaging (ESI) and diffraction (ESD) and different modes of EELS. This review summarizes the possibilities and prospects in the field of materials science.

2. Instrumentation for combined ESI, ESD and EELS.

Without discussing an electron filter lens in detail, we can look on such an electron optical device as a black box with the following conjugated planes in front of and behind the filter lens (Fig. 1) [18-21]. The filter entrance plane (FEP) contains a magnified bright-field (BF) or dark-field (DF) image for electron spectroscopic imaging(ESI) or a selected area diffraction pattern (SAED) for the electron spectroscopic diffraction (ESD), and this plane is conjugated to the achromatic image plane (AIP) with a 1:1 magnification. In this plane all electrons from one point of the FEP are focused in one point of the AIP regardless of their energy loss. However, electrons with increasing energy losses pass the image point under increasing angles ϵ to the optic axis. All electrons of the same energy loss are focused in one point of the energy-dispersive plane (EDP) where the electron energy-loss spectrum (EELS) can be observed. This plane is conjugated to the source plane SP at the focal plane of the first projector lens P1.This plane contains a demagnified diffraction pattern with a shadow of the objective diaphragm (OD) in case of ESI and a demagnified image shadowed by the selected area (SA) in case of ESD. As a consequence, the EELS in the EDP is convolved by the intensity distribution in these demagnified source images, which decrease in diameter with increasing magnification of the pre-filter optics. The projector lens P2 can either image the AIP or the EDP on the final image plane (FIP) containing a fluorescent screen for visual observation and a photographic emulsion or a digital recording system. A scintillator-photomultiplier combination below the camera chamber can be used for different modes of sequentially recorded EELS. A CCD array or SIT camera recording the intensity of an intermediate screen in front of or behind the camera chamber can be used for digital records of ESI and ESD or for parallel recorded EELS.

3. Electron spectroscopic imaging modes.

The electron spectroscopic imaging (ESI) mode is realized by a slit in the EDP to select an energy-loss window at an energy loss ΔE with a width $\delta E = $ 1-20 eV. The zero-loss peak of unscattered and elastically scattered electrons has been adjusted on axis. Increasing the accelerating voltage of the electron gun ($U = $ 80 kV) by ΔU shifts the EELS at the EDP and electrons with an energy loss $\Delta E = e\Delta U$ and an energy U will be on axis and pass the slit. Consequently, everytime 80 keV electrons are on axis between specimen and final screen. The focal change in the illumination system by varying U is compensated by varying the condensor lens currents. An unfiltered image can be recorded by withdrawing the slit in the EDP. A difference to a conventional image without filter lens will only be expected for thick specimens with a broad energy-loss spectrum when the electrons pass the AIP and P2 under larger angles to the optic axis and because only a total energy-loss width of the order of 200 eV passes the filter lens.

The different modes of ESI are demonstrated in the schematical EELS of a thin and thick specimen (Fig. 2) and will be discussed by examples from materials science.

3.1 ZERO-LOSS FILTERING. — The influence of zero-loss filtering on the transmission of amorphous and fine-crystalline carbon, germanium and platinum films [21-23] showed that the zero-loss filtered transmission $T_{\text{fil}}(\alpha)$ superposed of the unscattered and elastically scattered electrons through $0 \leq \theta \leq \alpha$ ($\alpha = $ objective aperture) shows an exponential decrease which for small α is identical with the decrease of the intensity of unscattered electrons

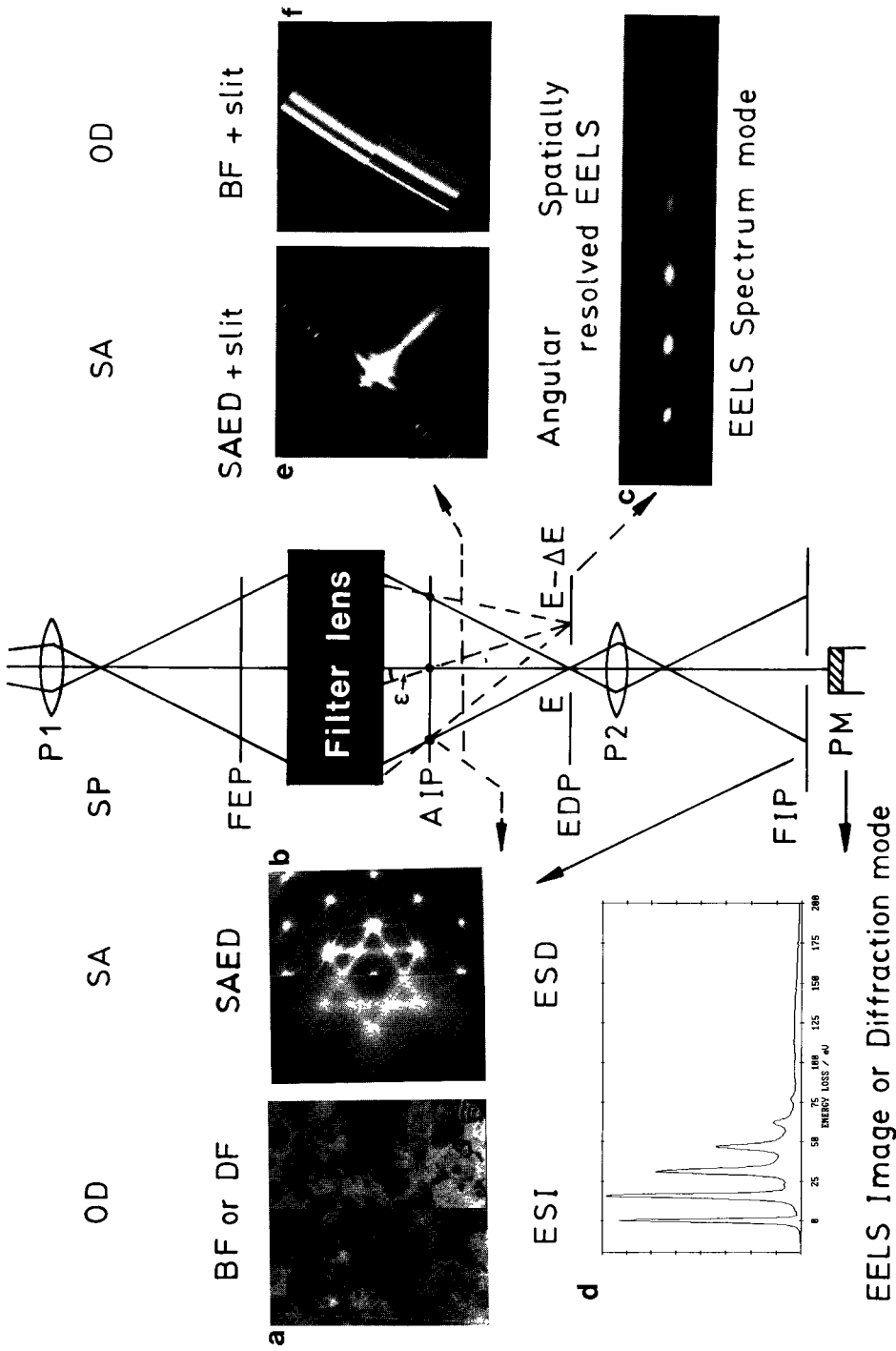$$T_{\text{fil}} = \exp\left[-x(1+\nu)/x_{\text{el}}\right] \tag{1}$$

Fig. 1. — Schematical ray path of a filter lens in an energy-filtering transmission electron microscope (P1, P2 projector lenses, SP source plane, FEP filter entrance plane, AIP achromatic image plane, EDP energy dispersive plane, FIP final image plane, PM scintillator-photomultiplier). Examples of a) electron spectroscopic imaging (ESI) of a 420 nm evaporated Al film unfiltered (left) and zero-loss filtered (right), b) electron spectroscopic diffraction (ESD) of a [111] oriented Si foil unfiltered (left) and zero-loss filtered (right), c) EELS of 40 nm Al foil recorded in the spectrum mode, d) EELS image mode (150 nm Al with plasmon losses and convolved L edge), e) angular resolved EELS (40 nm Al) and f) spatially resolved EELS (graphite crystal (right) on carbon film (left)).
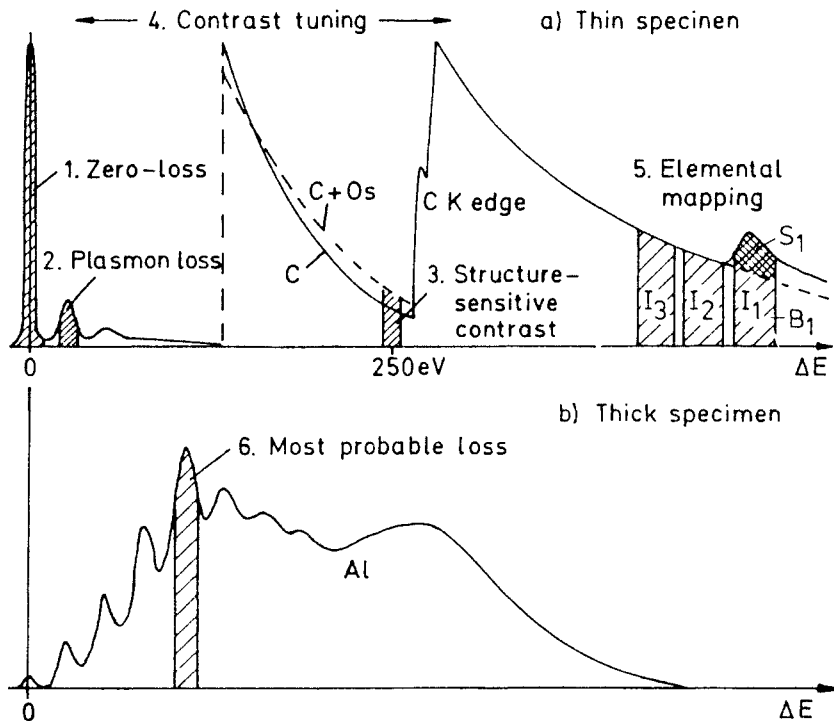
Fig. 2. — Electron Spectroscopic Imaging modes selecting electrons with different energy losses.

with increasing mass-thickness $x = \rho t$ (x_{el} = mean free path of elastic scattering) and is much lower than the unfiltered transmission $T_{unf}(\alpha)$ for carbon whereas the differences in T_{fil} und T_{unf} are lower in platinum films due to the ratio of inelastic-to-elastic total cross-sections [24, 25]

$$\nu = \sigma_{in}/\sigma_{el} \simeq 20/Z. \tag{2}$$

The useful mass-thicknesses for amorphous and fine-crystalline films of C, Ge and Pt which show a transmission of 10^{-3} as a practical limit for reasonable exposure times are 70-90 $\mu g/cm^2$ for $\alpha = 4$ mrad at $E = 80$ keV [23]. As an application of zero-loss filtering on amorphous specimens in materials science figure 3 shows unfiltered and zero-loss filtered images of a polyethylene-polypropylene copolymer stained with ruthenium oxide.

Coarse-crystalline films can easily be prepared to measure the maximum useful thickness for zero-loss imaging of single-crystal and large-grained crystalline specimens. Fig. 1a shows a comparison of an unfiltered and a zero-loss filtered ESI of a 420 nm aluminium film. When plotting semi-logarithmically the zero-loss transmission T_{fil} *versus* the mass-thickness $x = \rho t$ (Fig. 4), the averaged transmission over crystals of random orientations can be approximated by a single straight line (exponential decrease of transmission) with a value of $x = 150$ $\mu g/cm^2$ (550 nm Al or 75 nm Au) for $T_{fil} = 10^{-3}$ and $E = 80$ keV which is a practical limit for observing the image on the fluorescent screen and recording on a photographic emulsion with exposure times ≤ 100 s. The results of figure 4 can be described by [26]

$$T_{fil} = \exp\left[-2\pi t/\xi_0'\right] \quad ; \quad \xi_0' = h^2/2m\lambda V_0' \tag{3}$$

with the mean absorption length ξ_0' of dynamical theory and the imaginary zero Fourier coefficient V_0' of the lattice potential.
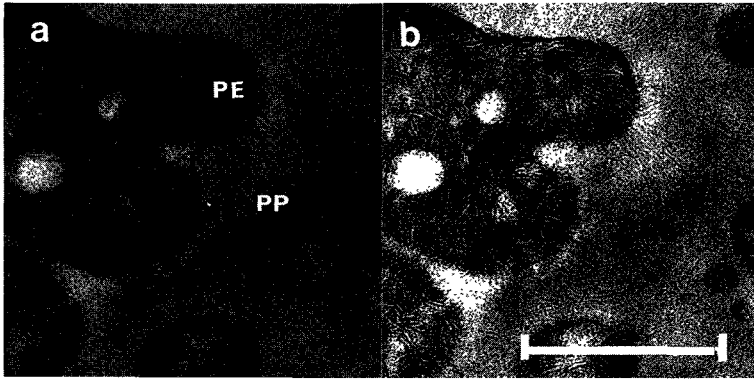
Fig. 3. — a) Unfiltered and b) zero-loss filtered image of a thin section of a copolymer of polyethylene (PE) and polypropylene (PP) stained with ruthenium oxide (bar = 0.5 μm).
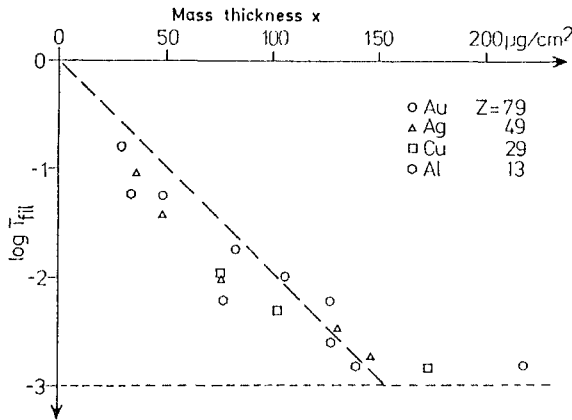

Fig. 4. — Mean transmission T_{fil} of evaporated metal films *versus* mass thickness $x = \rho t$.

These maximum mass-thicknesses of 150 μg/cm^2 are of the order of twice of those reported above for amorphous films. Such an increase in transmission for single-crystal and coarse-crystalline films compared to amorphous and fine-crystalline films has already been observed for the unfiltered transmission [27] and can be attributed to the averaging over areas with Bragg reflection and anomalous transmission and the destructive interference of elastic scattering in the absence of low-indexed Bragg reflections whereas the kinematical theory of electron diffraction is a good approximation for the fine-crystalline films. Anomalous transmission also allows to observe thicker single-crystal gold films [28]. The decrease of chromatic aberration by zero-loss filtering at 80 keV results in comparable images in a conventional TEM at 200 keV [29].

The theory of Bragg contrast of crystalline foils and of crystal-lattice imaging uses the interference of elastically scattered electrons. Though the next section demonstrates that Bragg contrast of thickness fringes and bend contours or of lattice defects is preserved in images by plasmon and higher energy losses, inelastic scattering results in a blurring of Bragg contrast and in chromatic aberration. Therefore, zero-loss filtering can remove the inelastic background and will allow a

better comparison with Bragg contrast calculated with the dynamical theory of electron diffraction. Figure 5 shows as an example the unfiltered (a) and zero-loss filtered (b) images of the Moiré structures in a cleaved graphite foil of $\simeq$ 500 nm.
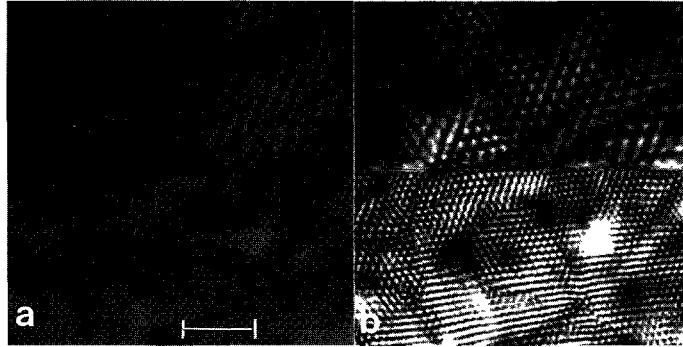

Fig. 5. — a) Unfiltered and b) zero-loss filtered image of a cleaved image graphite foil ($\simeq$ 500 nm) with Moiré fringes (bar = 1 μm).

3.2 PLASMON-LOSS FILTERING. — The filtering of plasmon losses can be used either to investigate the theory of image formation by plasmon losses or for a selective imaging of phases which differ in their plasmon losses more than 1 eV.

We know from theory [30, 31] and experiments [32-37] that the Bragg contrast is preserved in elastic scattering processes that excite plasmons or inner-shell ionizations of low ionization energy whereas elastic scattering between the Bragg spots caused by thermal-diffuse scattering shows a non-preservation of Bragg contrast. Therefore, plasmon loss-filtering shows approximately the same Bragg contrast in edge and bend contours and lattice-defect images as zero-loss filtering in the bright- and dark-field modes. When plasmon-scattered electrons are selected with a small objective diaphragm near the primary or Bragg spots the same bright- or dark-field images can be observed, whereas zero-loss filtering of the thermal-diffusely scattered electrons show no Bragg contrast but only contrat by anomalous absorption effects because their intensity between the spots is proportional to the probability density $\psi\psi^*$ of the Bloch wave field near the nuclei [26]. Also plasmon-loss filtering between the spots only shows anomalous absorption effects and no Bragg contrast, because these electrons are predominately elastically and inelastically double-scattered.

When increasing the energy loss an increased blurring of the high-order bend contours and thickness fringes has been observed [26, 37-41]. This can be explained by the angular distribution of inelastic scattering, which becomes equivalent to a spectrum of excitation errors. The differential scattering cross-section of plasmon losses ΔE_{pl}

$$\left[\frac{d\sigma}{d\Omega}\right]_{pl} = \frac{\Delta E_{pl}}{4\pi a_H} \frac{1}{N_e} \frac{1}{E} \frac{1}{\theta^2 + \theta_E^2} \tag{4}$$

(a_H = Bohr radius, N_e = number of valence electrons per unit volume) shows a small half-width of $\theta_E \simeq \Delta E/2E$ ($\simeq$ 0.1 mrad for $\Delta E = 16$ eV and $E = 80$ keV) which is much smaller than the usual illumination aperture of the order of 1-2 mrad. However, the Lorentzian function of $d\sigma(\theta)/d\Omega$

decreases slowly at larger θ up to the cut-off angle θ_c ($\simeq 6$ mrad for Al) and a large fraction of inelastically scattered electrons contributes to the increase of the effective illumination aperture and the spectrum of excitation errors. The convolution of two-beam dynamical calculations of edge contours with the angular distribution (4) of plasmon losses qualitatively confirm this blurring effect [26, 39].

Stacking fault contrast fringes have been observed up to $\Delta E = 300$ eV [26, 36] which can be explained by the relative insensitivity to excitation errors because the bright-field contrast is symmetric and starts at top and bottom with bright and dark fringes for $\alpha = +2\pi/3$ and $-2\pi/3$ faults, respectively.

Normally different phases or precipitates and matrix show differences in their plasmon-loss spectrum. In EELS these can be used for the identification of phases and the measurement of concentration of alloys with an accuracy of 0.1 eV in the plasmon shift (see Sect. 5.1 and Fig. 6c). In the ESI mode phases with sharp plasmon losses of an energy width smaller than 1 eV and separated by more than 1 eV can be selectively imaged when using a selecting energy window of $\delta E \simeq 1$ eV. For example, He bubbles in aluminium appear bright at $\Delta E = 11$ eV and disappear at the plasmon loss 15 eV of aluminium [42]; brighter images of Be precipitates in Al can be observed at 19 eV, the plasmon loss of Be [43]; crystals of In and Sn in a double layer ($\Delta E = 12$ and 13 eV) [20] or Al_3Li precipitates and Al-7wt%Li matrix ($\Delta E = 13.5$ and 14.5 eV) [44, 45] can be selectively increased in brightness. Figure 6a demonstrates that an unfiltered image of Al-7wt%Li shows a very weak contrast of the precipitates whereas these are imaged with a bright contrast in a plasmon-loss filtered image with the energy loss $\Delta E = 13.5$ eV of the $AlLi_3$ precipitates (Fig. 6b) and a dark contrast with the energy loss $\Delta E = 14.5$ eV of the plasmon loss of the Al matrix (Fig. 6d) when using an energy window with a width $\delta E = 1$ eV. The parallel-recorded EELS in Fig. 6c demonstrates that the sharpness of the plasmon losses is sufficient for this separation of phases.

3.3 STRUCTURE-SENSITIVE IMAGING.

— In biological specimens ESI with an energy window at $\Delta E \simeq 250$ eV just below the carbon K edge will show the minimum contribution of carbon to the image intensity. The image intensity from structures containing other elements like phosphorus and heavy metal atoms from fixation and staining is considerably increased with a dark-field-like contrast much higher than a conventional dark-field image [25, 46, 47].

This type of contrast is not restricted to biological sections. In doubly evaporated Ag-Au films on rocksalt, the Ag crystals appear bright just beyond the Ag $M_{4,5}$ edge at $\Delta E = 440$ eV and the Au crystals appear brighter below the edge where the contribution of Ag is a minimum as it is for C below the C K edge [48].

3.4 CONTRAST TUNING.

— The EELS from different parts of a specimen can intersect several times due to differences in the decrease of the background intensity with increasing energy loss and overlapped ionisation edges. This causes contrast reversals when tuning the selected energy over a large range of ΔE. This technique of contrast tuning [49, 50] has been applied to thicker biological sections when stained areas become very dark and cannot be recorded together with brighter areas due to the limited range of grey levels of photographic emulsions. Tuning the energy can result in an optimum condition to record both parts with comparable contrast and intensity.

Figure 7 shows an example of contrast tuning for selectively increasing the contrast in the same copolymer as shown in figure 3 but with less ruthenium oxide and a thicker section. The unfiltered image (Fig. 7a) and the ESI at $\Delta E = 50$ eV (Fig. 7b) shows no strong difference in contrast and the boundary of phases cannot clearly be identified. A maximum contrast and a good separation of polyethylene and polypropylene can be obtained with $\Delta E = 200$-250 eV (Fig. 7c). This contrast decreases at $\Delta E = 350$ eV (Fig. 7d) beyond the carbon K edge.
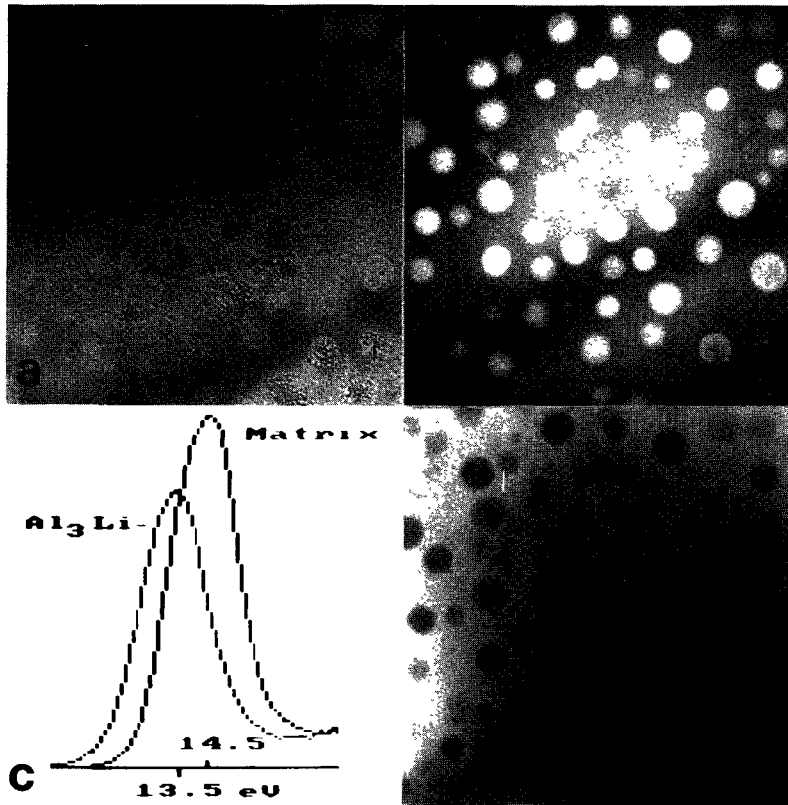
Fig. 6. — Plasmon-loss filtering of an Al-7wt%Li alloy with spherical Al_3Li precipitates, a) unfiltered bright-field image, b) $\Delta E = 13.5$ eV (plasmon loss of $AlLi_3$), c) parallel-recorded EELS of matrix and precipitates, d) $\Delta E = 14.5$ eV (plasmon loss of Al matrix) (bar = 100 nm).

3.5 ELEMENTAL MAPPING. — When subtracting pixel per pixel the extrapolated background intensity from the ESI at an energy loss just beyond the ionisation energy of an element of interest this net image can be considered as an elemental map [51]. The background can be extrapolated by two ESI below the edge [52, 53] or by one below and the other beyond a white line (e.g. Ca L) [54].

The EELS and ESI net intensity within an energy window ΔE, $\Delta E + \delta E$ can be written

$$I_n = I_0(\delta E, \alpha)\sigma(\delta E, \alpha)N \tag{5}$$

with N = number of the atoms of the element per pixel, $\sigma(\delta E, \alpha)$ = partial cross-section of ionisation and $I_0(\delta E, \alpha)$ = image intensity in a low-loss image including the zero-loss. For quantitative EELS and elemental mapping, the partial cross-sections has to be known by calibration experiments. An important problem is the decrease of intensities I_0 and I_n when electrons are scattered through angles larger than the objective aperture α[53, 55]. For example, the net intensity in elemental maps of Ca in epon sections of Ca-phosphate crystals in the pre-stage of bone mineralization is decreased by the stronger elastic large-angle scattering of Ca. As a consequence, non-specific intensities from the surrounding cell structure become comparable in intensity. When taking a fourth image at low losses inclusively the zero-loss (I_0) a digital division I_n/I_0 results in
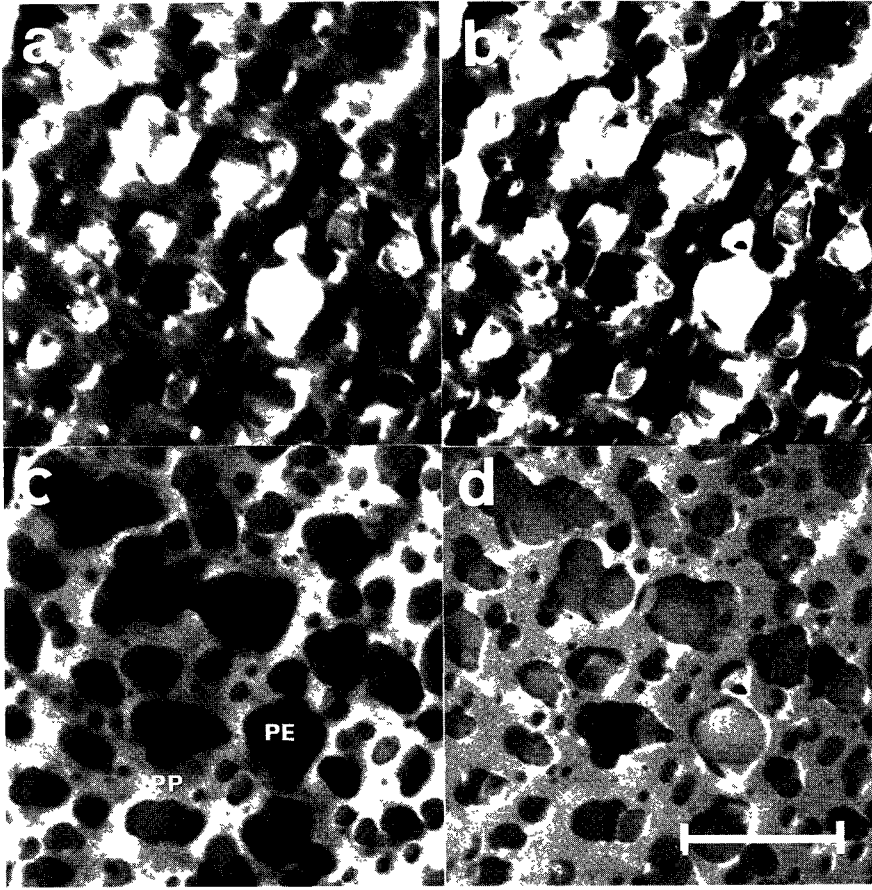
Fig. 7. — Copolymer of polyethylene (PE) and polypropylene (PP) stained with less ruthenium oxide and a thicker section than in figure 3: a) unfiltered, b) $\Delta E = 50$ eV, c) $\Delta E = 200$ eV, d) $\Delta E = 350$ eV (bar = 5 μm).

a stronger increase of the Ca containing structures relative to the other structures not containing Ca [56]. In crystalline specimens, I_0 and I_n can be decreased very strongly by Bragg reflection and due to the blurring of Bragg contrast in ESI at higher energy losses (Sect. 3.2) the division by I_0 will show less success. Because the foil thikness should be smaller than the mean-free-path of plasmon losses, thinner foil thicknesses are necessary for an elemental mapping of solids [56-58] than for biological sections and a large interest exist for EFTEM at higher voltages.

3.6 MOST-PROBABLE-LOSS IMAGING. — When the zero-loss transmission T_{fil} falls below 10^{-2} the EELS consists of a broad Landau maximum formed by multiple plasmon losses and convolved ionisation edges. Up to mass-thicknesses $x \simeq 300$ μg/cm^2 the intensity in a $\delta E = 5$-10 eV window at the most-probable energy loss is larger than 10^{-3} of the incident intensity and can be used for most-probable-loss imaging, [26, 59, 60]. This avoids the very strong chromatic aberration. The multiple scattering in such thick films fills the range of scattering angles $0 \leq \theta \leq \alpha_0$ (α_0 = objective aperture) with approximately constant intensity. As discussed in section 3.2 for plasmon losses this results in a very broad spectrum of excitation errors. The situation is comparable with the

STEM mode of a TEM working with a large probe and detector aperture [61-65]. Edge and bend contours decrease very strongly in contrast. However, differences in crystal orientation by bending or at grain boundaries and even lattice defects can still cause a contrast due to differences in anomalous absorption.

For very thick specimens ($\simeq$ 1 μm for polystyrene and 0.5 μm for aluminium) a top-bottom effect caused by multiple scattering has to be taken into account [66] which is reciprocal to the top-bottom effect in the STEM mode [67] but reduced in magnitude.

4. Electron spectroscopic diffraction modes.

4.1 AMORPHOUS SPECIMENS. — The diffraction patterns of amorphous specimens show diffuse diffraction maxima and minima. A Fourier transform of the oscillations around the averaged decrease of elastic scattering expected without interference results in the radial density distribution $4\pi r^2 \rho(r) dr$ of atoms with distances r, $r+dr$ [68, 69] which is of interest to investigate the structure of different amorphous semiconducting and metallic films. For a more quantitative interpretation it is important to select only the elastically scattered electron by energy filtering. Using scanning (Grigson) coils below P2 the zero-loss filtered diffraction pattern can be scanned across the diaphragm of the scintillator – photomultiplier system for a sequential radial record.

4.2 SMALL-ANGLE ELECTRON DIFFRACTION. — In contrary to small-angle x-ray diffraction the corresponding diffraction method for electrons [70-72] is handicapped by the superposition of inelastic small-angle scattering which shows no diffraction for periods larger than the diameter of the excitation volume of plasmon losses of the order of 1 nm [73]. Therefore, zero-loss filtering has successfully been applied to decrease the inelastic background [74, 75] in small-angle diffraction patterns of evaporated films. The diameter of the halo allows to get a statistical information about the distribution of particle distance. In future zero-loss filtering should also allow to get quantitative information about the radius of gyration as a measure of the size of particles from the decrease of diffuse scattering, especially when the illumination aperture and the analysed area can be decreased by the use of field emission guns.

4.3 POLYCRYSTALLINE DIFFRACTION PATTERNS. — Increasing thickness of polycristalline films results in an increase of inelastic background and a decrease of the peak intensity of Debye-Scherrer rings. Zero-loss filtering allows to record Debye-Scherrer rings from $\simeq$ 0.5 μm aluminium films with 80 keV electrons which show no rings in unfiltered diffraction patterns. The benefit of zero-loss filtering can be recognized by measurements of the gain in peak-to-background ratios for increasing thickness of evaporated aluminium films (Fig. 8), see also measurements of CaF_2 on carbon in [76].

4.4 SINGLE-CRYSTAL DIFFRACTION PATTERNS. — Energy filtering of single-crystal diffraction patterns [18, 19, 21, 73, 77-82] can be used for a contrast enhancement of Bragg spots, thermal-diffuse streaks caused by electron-phonon scattering and Kikuchi lines and bands by zero-loss filtering and for a separation of the contributions of plasmon scattering to Kikuchi lines and bands and inner-shell ionization processes. Figure 1b shows the unfiltered (left) and zero-loss diffraction patterns of a 111-oriented Si foil and Figure 9 shows a series of (a) unfiltered and (b-f) energy-filtered diffraction patterns of an 100-oriented GaAs-foil. The zero-loss image (b) decreases the inelastic background and results in a better contrast of thermal-diffuse streaks, Kikuchi lines and weak, forbidden reflections from the first Laue zone. With thin foils, the thermal-diffuse streaks caused by electron-phonon scattering [83, 84] only appear in the zero-loss image, whereas
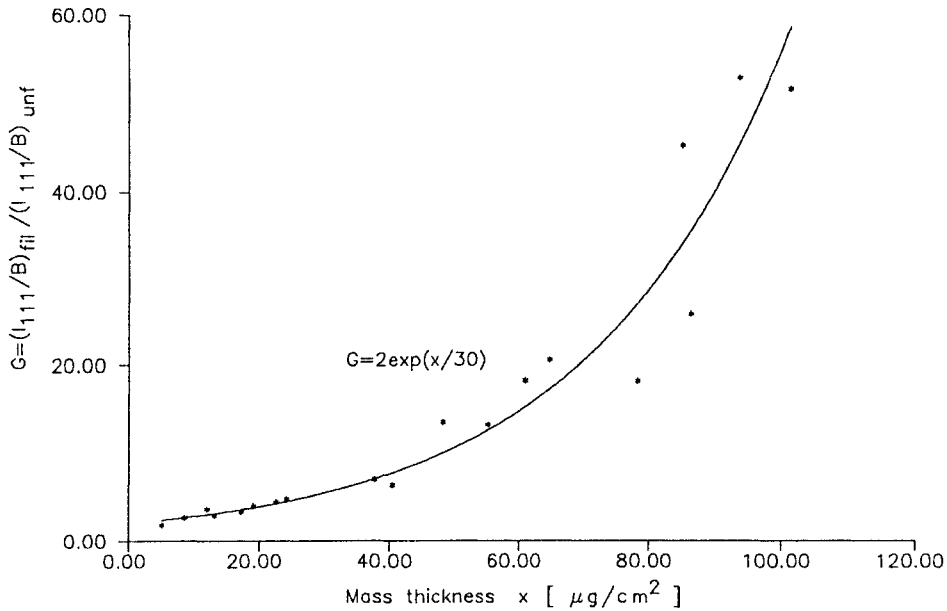
Fig. 8. — Increase in the ratio (gain G) of ring peak to background ratios in zero-loss filtered and unfiltered Debye-Scherrer diffraction patterns of evaporated aluminium films with increasing film thickness.

in thicker foils they also appear in the plasmon-loss images due to elastic-inelastic double scattering. The Bragg spots are increasingly blurred with increasing energy loss by a convolution with the angular distribution of inelastically scattered electrons and disappear at energy losses of a few hundreds of eV. However, excess and/or defect Kikuchis bands can be observed up to energy losses of a few thousands of eV. When the contribution to the observed high energy loss in the EELS is predominately caused by a single ionization loss from the plasmon-loss region to an energy loss beyond the Ga and As L_{23} edges at 1115 eV and 1323 eV, excess Kikuchi bands are observed, because the probability for scattering into a distinct direction of the diffraction pattern is proportional to the probability density of a Bloch wave at the nuclei (inner shells) of the outgoing wave direction. Figures 9e below and 9f beyond the edges demonstrate the increase in contrast of Kikuchi bands and lines. In case of thick foils the upper part of the foil acts as a diffusing medium and the broad angular distribution results in defect Kikuchis band caused by anomalous absorption [85]. For foils with medium thickness the contrast of Kikuchi bands change from defect at low to excess at high energy losses [21, 73].

4.5 TWO-DIMENSIONAL MAPPING OF PLASMON-LOSS DISPERSION AND COMPTON SCATTERING. —
The angular distribution of inelastic scattering due to interband transitions, plasmon losses and Compton scattering results in special contrast effects in energy-filtered diffraction patterns. When filtering with $\delta E \simeq 1$ eV in small increasing steps of energy loss a bright disc around the primary beam and the Bragg spots appear just beyond the plasmon loss due to the angular distribution (4). When the plasmon loss shows a dispersion as a parabolic increase of the plasmon energy with increasing scattering angle, the disc becomes a diffuse ring of increasing diameter when increasing the selected energy loss [44] and the ring disappears when the scattering angle reaches the cut-off angle (Fig. 10). The dispersion of plasmon losses and interband transitions shows a crystal anisotropy [86, 87] which can be images by this method in a two-dimensional map of iso-
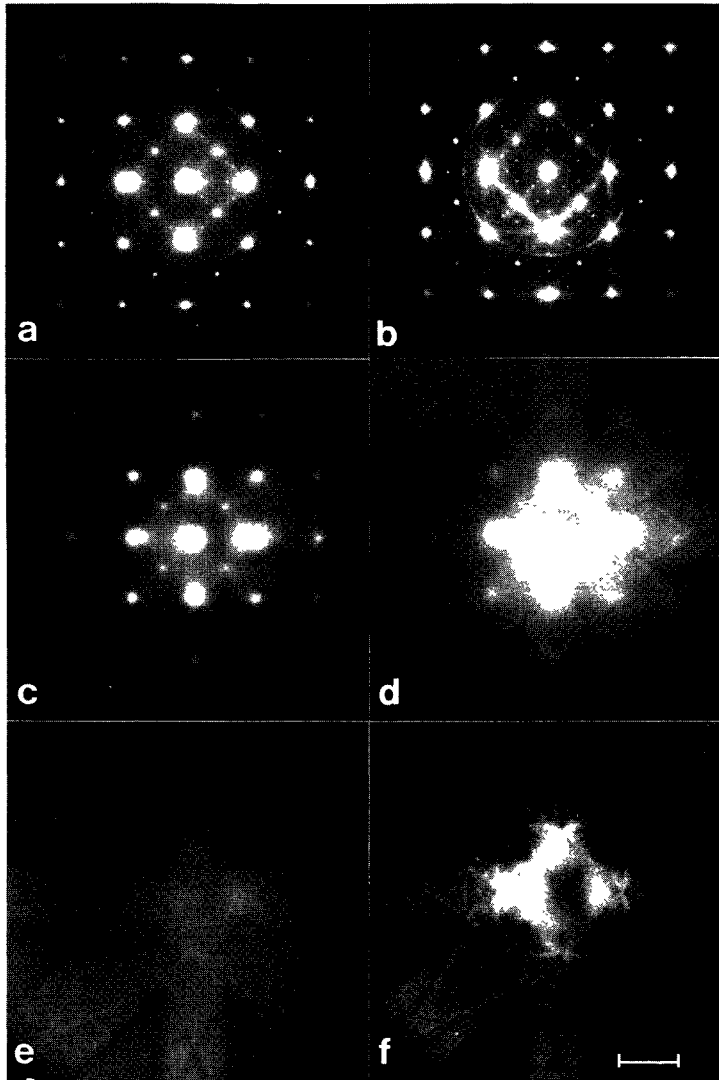
Fig. 9. — Electron spectroscopic diffraction (ESD) patterns of single-crystal GaAs: a) unfiltered, b) zero-loss filtered, c) $\Delta E = 100$ eV, d) $\Delta E = 300$ eV, e) $\Delta E = 1000$ eV and f) $\Delta E = 1335$ eV (bar = 20 mrad).

densities [44] as deviations from concentric isodensities which should appear in case of isotropic dispersion. This is demonstrated in figure 11 for the case of the interband transition of graphite. The isodensities at $\Delta E = 7$ eV (Fig. 10a) and 13 eV (Fig. 10b) show a hexagonal shape with the corners directed to the Bragg reflection (a) and between the reflection in (b). The plasmon loss at $\Delta E \pm 31$ eV shows an isotropic dispersion (Fig. 10c). Contrary to this method of mapping with a lot of scattering angles and azimuths, a series of EELS at different scattering angles and only two azimuths [86] had to be used to analyze this anisotropy. Therefore, this technique can become an additional analytical method.
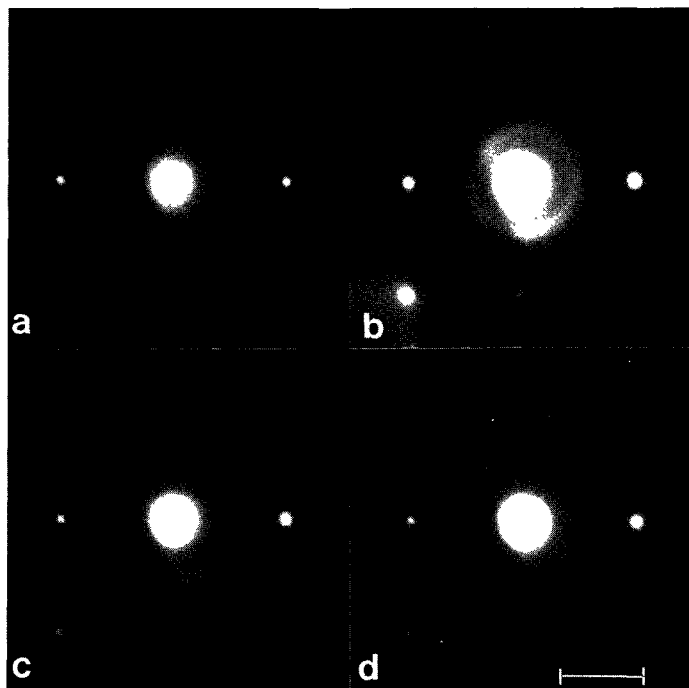
Fig. 10. — ESD pattern of a single-crystalline evaporated Sn film at a) $\Delta E = 18$ eV, b) 20 eV, c) 23 eV and d) 28 eV showing diffuse rings caused by the dispersion of plasmon loss (bar = 10 mrad).
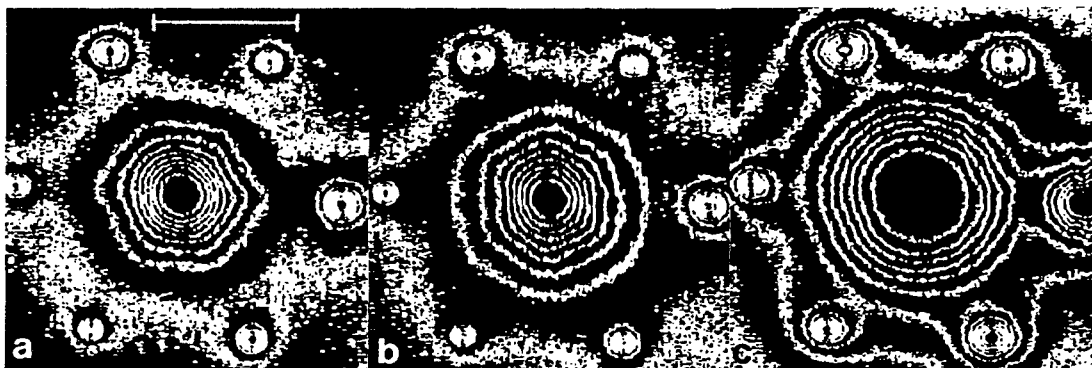

Fig. 11. — Isodensities of ESD patterns of a graphite foil showing the anisotropies for the interband transition losses at a) $\Delta E = 7$ eV and b) $\Delta E = 13$ eV and no anisotropy for the c) plasmon loss at $\Delta E = 31$ eV (Electron beam parallel c-axis, bar = 20 mrad).

When increasing the filtered energy loss to a few hundreds of eV a new brighter circle appears which increases in diameter proportional to the square root of energy loss and can be attributed

to the Compton scattering [88, 89] with a maximum (Bethe ridge) at the Compton angle

$$\sin^2 \theta_C = \Delta E / E \left[1 + \frac{E - \Delta E}{2 \, m_0 \, c^2} \right]^{-1} .$$

(6)

In figure 12 we confirm this relation by a plot of θ_C^2 *versus* ΔE for aluminium and different carbon modifications. Systematic lower value of θ_C and the high extrapolated value of $\Delta E = 80$ eV for $\theta_C = 0$ has also been reported for amorphous carbon by Egerton [88] and cannot be explained by theory whereas the measured θ_C values of graphite are systematically higher and the extrapolation to $\theta_C = 0$ only shows an intersection of a few volts because the energies in the band structure of graphite are only 6 eV and 25 eV below the vacuum level [90]. IN EFTEM the Compton peak can be recorded by ESD pattern at an energy loss of a few hundreds of eV on a photographic emulsion, by a radial linescan across the diffraction pattern using Grigson coils or by a small diaphragm at a fixed large scattering angle of the order of 100 mrad and varying the selected energy loss.
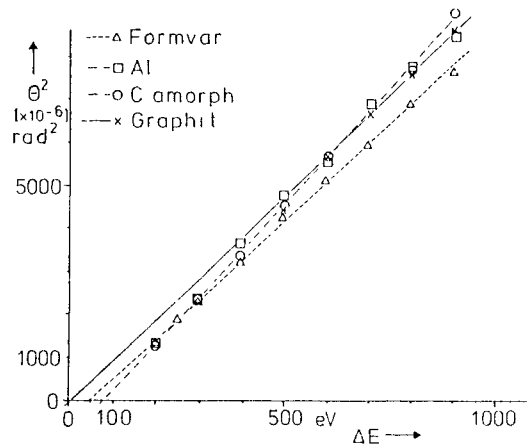

Fig. 12. — Measured values of the Compton angle θ_C (maximum of Bethe ridge) with increasing energy loss ΔE for graphite, formvar, amorphous carbon and aluminium, showing deviations from equation (6).

5. EELS modes.

5.1 EELS SPECTRUM MODE. — The magnification of the EDP on the fluorescent screen by P2 results in an EELS spectrum (Fig. 1c) which can be recorded on a photographic emulsion, sequentially by scanning the spectrum across a slit in front of a scintillator-photomultiplier combination below the camera (Fig. 1d), or parallel-recorded by a fluorescent screen coupled to a CCD or SIT camera. Figure 6c shows two parallel-recorded plasmon loss spectra from the Al matrix ($\Delta E = 14.5$ eV) and a Al_3Li precipitate ($\Delta E = 13.5$ eV). It is possible to determine the position of the loss with an accuracy of 0.1 eV though the resolution is only of the order of 1 eV due to the energy spread of the thermionic electron gun.

5.2 EELS IMAGE AND DIFFRACTION MODES. — In this mode either the ESI or ESD mode is used with a filtered bright-field image or selected-area electron diffraction pattern on the fluorescent screen. When increasing the acceleration voltage continuously in steps of 0.5 eV the EELS in the EDP shifts over the energy-selecting slit and the ESI or ESD in the final image varies in intensity but does not shift. A small diaphragm in front of the scintillator-photomultiplier can select a small specimen area of diameter d/M depending on the diameter d of the diaphragm and the magnification M and the sequential record of ESI intensity represents the EELS of the selected area (EELS image mode). In the EELS diffraction mode, the filtered diffraction patterns can be shifted by deflection coils which allows to record EELS at different scattering angles with an angular diameter $\Delta\theta = d/L$ and a solid angle $\Delta\Omega = \pi(d/L)^2/4$ depending on the diaphragm d and the camera length L of the diffraction pattern. This can be used to investigate the shift of the plasmon loss with increasing scattering angle due to plasmon dispersion or of the Compton profile (Bethe ridge) at large scattering angles.

5.3 SPATIALY AND ANGULAR-RESOLVED EELS. — When selecting a line in an image or a diffraction pattern by a slit of $\simeq$ 1-2 μm in the FEP which is perpendicular to the direction of EELS in the EDP, defocusing of P2 relative to the AIP (dashed plane in Fig. 1) results in a continuous set of EELS patterns from each point of the selected line [91]. This technique has been used for a spatially-resolved EELS with the slit across different phases or precipitates [92, 93] or for an angular-resolved EELS with the slit across a diffraction pattern [94-97]. The angular resolved EELS from an evaporated aluminium film (150 nm) in figure 1e shows the zero-loss line with the primary beam and Debye-Scherrer rings and the 15 eV plasmon loss and its dispersion (parabolic curvature) and the Al L losses beyond 75 eV. In the spatially-resolved EELS of figure 1f, the slit runs across a graphite flake (bottom) on a carbon supporting film (top). The shift of the plasmon loss from 23 eV (carbon) to 27 eV (graphite) and the appearance of the 7 eV loss of graphite can be clearly identified.

References

[1] BOERSCH H., *Naturwiss* 35 (1948) 26; *Z. Phys.* **134** (1953) 156.

[2] MÖLLENSTEDT G. and RANG O., *Z. Angew. Phys.* **3** (1951) 187.

[3] MÖLLENSTEDT G., *Optik* **5** (1949) 499.

[4] RAETHER H., Excitation of Plasmons and Interband Transitions by Electrons.
Springer Tracts in Modern Physics, Vol. 88 (Springer, Berlin, Heildelberg, New York, 1980).

[5] BOERSCH H., GEIGER J. and HELWIG H., *Phys. Lett.* **3** (1962) 64.

[6] GEIGER J., NOLTING M. and SCHRÖDER B., Microscopie Electronique 1970, Vol. 1, Soc. Française Micr. Electr. (Paris, 1970) p. 111.

[7] RUDBERG E., *Proc. Roy. Soc. London A* **127** (1930) 111.

[8] RUTHEMANN G., *Naturwiss* **29** (1941) 648; **30** (1942) 145.

[9] HILLIER J. and BAKER R.F., *J. Appl. Phys.* **15** (1944) 663.

[10] COLLIEX C., Adv. in Optical and Electron Microscopy, Vol. 9, R. Barer and V.E. Cosslett Eds. (Academic Press, London, 1984) p. 65.

[11] EGERTON R.F., Electron Energy-loss Spectroscopy in the Electron Microscope (Plenum Press, New York, London, 1986).

[12] CASTAING R. and HENRY L., *C. R. Acad. Sci. Paris* **255** (1962) 76.

[13] HENKELMAN R.M. and OTTENSMEYER F.P., *J. Micr.* **102** (1974) 79.

[14] EGLE W., RILK A., and OTTENSMEYER F.P., Electron Microscopy (1984), Proc. 8th Europ. Congr. on Electr. Micr., Vol. I, A. Csanády, P. Röhlich and D. Szabó, Eds. Budapest (1984) p. 63.

[15] ROSE H., and PLIES E., *Optik* **40** (1974) 336.

[16] LANIO S., *Optik* **73** (1986) 99.

[17] LANIO S., ROSE H. and KRAHL D., *Optik* **73** (1986) 56.

[18] CASTAING R., *Z. Angew.Phys.* **27** (1969) 171.

[19] REIMER L., FROMM I. and RENNEKAMP R., *Ultramicroscopy* **24** (1988) 339.

[20] REIMER L., BAKENFELDER A., FROMM I., RENNEKAMP R. and ROSS-MESSENER M., *EMSA Bull.* **20** (1990) 73.

[21] REIMER L., *Adv. Electr. Electr. Electron Physics* Vol. 81 (Academic Press, Boston, 1981) p. 43

[22] REIMER L., ROSS-MESSENER M., *Inst. Phys. Conf. Ser. No. 93*, Vol. 1, EUREM 88, York, England (1988) p. 181.

[23] REIMER L. and ROSS-MESSENER M., *J. Micr.* **155** (1989) 169.

[24] EGERTON R.F., *Phys. Status Solidi* (a) **37** (1976) 663.

[25] REIMER L. and ROSS-MESSEMER M., *J. Micr.* **159** (1990) 143.

[26] BAKENFELDER A., FROMM I., REIMER R. and RENNEKAMP R., *J. Micr.* **159** (1990) 161.

[27] REIMER L., *Naturwissenschaften* **49** (1962) 297; *Z. Angew. Phys.* **22** (1967) 287.

[28] LEHMPFUHL G., KRAHL D. and SWOBODA M., *Ultramicroscopy* **31** (1989) 161.

[29] BAKENFELDER A., REIMER L. and RENNEKAMP R., Proc. XIIth Int. Congr. for Electr. Micr., Vol. 2 (San Francisco Press, 1990) p. 62.

[30] HUMPHREYS C.J. and WHELAN M.J., *Philos. Mag.* **20** (1969) 165.

[31] HOWIE A., *Proc. Roy. Soc. A* **271** (1963) 268.

[32] WATANABE H., *Jpn. J. Appl. Phys.* **3** (1964) 480.

[33] CASTAING R., HENOC P., HENRY L. and NATTA M. *C. R. Acad. Sci. (Paris) B* **265** (1967) 1293.

[34] CUNDY S.L., METHERELL A.J.F. and WHELAN M.J., *Philos. Mag.* **15** (1967) 623.

[35] CUNDY S.L., HOWIE A. and VALDRE U., *Philos. Mag.* **15** (1967) 623.

[36] CRAVEN A.J., GIBSON J.M., HOWIE A. and SPALDING D.R., *Philos. Mag. A***38** (1978) 519.

[37] METHERELL A.J.F., *Philos. Mag.* **15** (1967) 763.

[38] DUVAL P. and HENRY L., *J. Appl. Cryst.* **6** (1977) 113.

[39] DONIACH S. and SOMMERS C., *Philos. Mag.* **51** (1985) 419.

[40] ROSSOUW C.J. and WHELAN M.J., *Ultramicroscopy* **6** (1981) 53.

[41] STOBBS W.M. and BOURDILLON A.J., *ultramicroscopy* **9** (1982) 303.

[42] HENOC P., NATTA M. and HENRY L., Microscopie Electronique, vol. 2 (Soc. Française Micr. Electr. Paris, 1970) p. 123.

[43] CASTAING R., Physical Aspects of Electron Microscopy and Microanalysis, R.J. Siegel and D.R. Beaman (John Wiley, New York, 1975) p. 287.

[44] FROMM I., REIMER L. and RENNEKAMP R., *J. Micr.* (in press).

[45] SAINFORT P. and GUYOT P., *Philos. Mag. A* **51** (1985) 575.

[46] PROBST W. and BAUER R., *Verh. Dtsch. Zool. Ges.* **80** (1987) 119.

[47] BAUER R., Methods in Microbiology, Vol. **20**, F. Mayer Ed. (Academic Press, London, 1988) p. 113.

[48] KEUSCH P., GUENTER J.R. and BAUER R., Proc. XIth Int. Congr. on Electr. Micr., Kyoto (1986) Vol.II, p. 1379.

[49] BAUER R., HEZEL U. and KURZ D., *Optik* **77** (1987) 171.

[50] WAGNER H.J., *Ultramicroscopy* **32** (1990) 42.

[51] ADAMSON-SHARPE K.M. and OTTENSMEYER F.P., *J. Micr.* **122** (1981) 309.

[52] OTTENSMEYER F.P., *Ann. New York Acad. Sci* **483** (1986) 339.

[53] SHUMAN H., CHANG C.F., BAHLE E.F. and SOMLYO A.P., *Ann. New York Acad. Sci.* **483** (1986) 295.

[54] COLLIEX C., *Ann. New York Acad. Sci.* **483** (1986) 311.

[55] LEAPMAN R.D., *Ann. New York Acad. Sci.* **483** (1986) 326.

[56] ZANCHI G., SEVELY J. and JOUFFREY B., *J. Micr. Spectr. Electron.* **2** (1977) 95.

[57] OTTENSMEYER F.P., ANDREWS D.W., ARSENAULT A.L., HENG Y., SIMON G.T. and WEATHERLEY G.C., *Scanning* **10** (1988) 227.

[58] BAUER R., PROST W. and MILLER W., Proc. 46th Ann. Meeting EMSA (San Francisco Press, 1988) p. 524.

[59] COLLIEX C., MORY C. OLINS A.L., OLINS D.E. and TENCE M., *J. Micr.* **153** (1989) 1.

[60] REIMER L., RENNEKAMP R., FROMM I. and LANGENFELD M., *J. Micr.* **162** (1991) 3.

[61] REIMER L., Scanning Electron Microscopy: systems and applications (Inst. of Physics, London, 1973) p. 120.

[62] BOOKER G.R., JOY D.C., SPENCER J.P. and von HARRACH H., Scanning Electron Microscopy (1974) IITRI, Chicago, p. 225.

[63] MAHER D.M. and JOY D.C., *Ultramicroscopy* **1** (1976) 239.

[64] REIMER L. and HAGEMANN P., Scanning Electron Microscopy 1976/I, IITRI, Chicago, p. 321.
[65] REIMER L. and HAGEMANN P., *Optik* **47** (1977) 325.
[66] REIMER L. and ROSS-MESSEMER M., *Ultramicroscopy* **21** (1987) 385.
[67] GENTSCH P., GILDE H. and REIMER L., *J. Micr.* **100** (1974) 81.
[68] LEONHARDT R. RICHTER H. and ROSSTEUTSCHER W., *Z. Phys.* **165** (1961) 12.
[69] COCKAYNE D.J.H. and MCKENZIE D.R., *Acta Cryst. A* **44** (1988) 870.
[70] MAHL H. and WEITSCH W., *Z. Naturforschg.* **15a** (1960) 1051.
[71] FERRIER R.P., Adv. in Optics and Electron Microscopy, Vol. 3, by R. Barer and V.E. Cosslett Eds. (Academic Press, London, 1969) p. 155.
[72] WADE R.H. and SILCOX J., *Phys. Status Solidi* **19** (1967) 57.
[73] REIMER L., FROMM I. and NAUNDORF I., *Ultramicroscopy* **32** (1990) 80.
[74] CASTAING R., *Z. angew. Phys.* **27** (1969) 171.
[75] DUVAL H. and HENRY L., *J. Appl. Cryst.* **6** (1973) 113.
[76] BARCKHAUS B.H., HÖHLING H.J., FROMM I., HIRSCH P. and REIMER L., *J. Micr.* **162** (1991) 155.
[77] CREUZBERG M. and DIMIGEN H., *Z. Phys.* **174** (1970) 1338.
[78] MEYER-EHMSEN G. and SIEMS G., *Phys. Status Solidi (b)* **63** (1974) 577.
[79] PHILIP J.G., WHELAN M.J. and EGERTON R.F., Electron Microscopy 1974, Australian Acad. od Science, Canberra (1974) Vol. I, p. 276.
[80] EGERTON R.F., PHILIP J.G., TURNER P.S. and WHELAN M.J. *J.Phys. E* **8** (1975) 1033.
[81] REIMER L. and FROMM I., Proc. 47th Ann. Meeting EMSA (San Francisco Press) p. 382.
[82] MAYER J., SPENCE J.C.H. and MÖBUS G., Proc. 49th Ann. Meeting EMSA (San Francisco Press, 1991) p. 786.
[83] HONJO G., KODERA S. and KITAMURA N. *J. Phys. Soc. Jpn* **19** (1964) 351.
[84] KOMATSU K. and TERAMOTO K., *J. Phys. Soc. Jpn* **21** (1966) 1152.
[85] REIMER L., SCANNING **2** (1979) 3.
[86] DANIELS J., FESTENBERG C. and RAETHER H., *Springer Tracts in Modern Physics* Vol. 4 (Springer, Berlin, Heidelberg, New York, 1970) p. 77.
[87] ZEPPENFELD K., *Z. Phys.* **211** (1968) 391; **243** (1971) 229.
[88] EGERTON R.F., *Philos. Mag.* **31** (1975) 199.
[89] WILLIAMS B.G., SPARROW T.C. and EGERTON R.F., *Proc. Roy Soc. A* **393** (1984) 409.
[90] PAINTER G.S. and ELLIS D.E., *Phys. Rev. B* **1** (1970) 4747.
[91] REIMER L. and RENNEKAMP R., *Ultramicroscopy* **28** (1989) 258.
[92] CUNDY S.L., METHERELL A.J.F. and WHELAN M.J., *Philos. Mag.* **15** (1967) 623; **17** (1968) 141.
[93] CUNDY S.L., HOWIE A. and VALDRE U., *Philos. Mag.* **20** (1969) 147.
[94] CAZAUX J., *J. Microsc.* **8** (1969) 637.
[95] LEONHARD F., *Z. Naturforschg.* **9a** (1954) 727 + 1019.
[96] METHERELL A.J.F., Adv. in Optical and electron Microscopy, Vol. 4, R. Barer and V.E. Cosslett Eds. (Academic Press, London, 1971) p. 263.
[97] CURTIS G.H. and SILCOX J., *Rev. Sci. Instrum.* **42** (1971) 630.